Karam Zadeh Toularoud, N., Heimann, S., Dahm, T., Krüger, F. (2019): Application based seismological array design by seismicity scenario modelling. - *Geophysical Journal International*, *216*, 3, pp. 1711—1727.

DOI: http://doi.org/10.1093/gji/ggy523

Geophysical Journal International

Geophys. J. Int. (2019) **216,** 1711–1727
Advance Access publication 2018 December 13
GJI Seismology

doi: 10.1093/gji/ggy523

Application based seismological array design by seismicity scenario modelling

N. Karamzadeh,[1,2] S. Heimann,[1] T. Dahm[1,2] and F. Krüger[2]

[1] *Physics of Earthquakes and Volcanoes, GFZ German Research Centre for Geosciences, Potsdam 14467, Germany. E-mail: karamzad@gfz-potsdam.de*
[2] *Institute of Earth and Environmental Science, University of Potsdam, Potsdam 14476, Germany*

Accepted 2018 December 12. Received 2018 December 10; in original form 2018 March 9

SUMMARY

The design of an array configuration is an important task in array seismology during experiment planning. Often the array response function (ARF), which depends on the relative position of array stations and frequency content of the incoming signals, is used as the array design criterion. In practice, additional constraints and parameters have to be taken into account, for example, land ownership, site-specific noise levels or characteristics of the seismic sources under investigation. In this study, a flexible array design framework is introduced that implements a customizable scenario modelling and optimization scheme by making use of synthetic seismograms. Using synthetic seismograms to evaluate array performance makes it possible to consider additional constraints. We suggest to use synthetic array beamforming as an array design criterion instead of the ARF. The objective function of the optimization scheme is defined according to the monitoring goals, and may consist of a number of subfunctions. The array design framework is exemplified by designing a seven-station small-scale array to monitor earthquake swarm activity in Northwest Bohemia/Vogtland in central Europe. Two subfunctions are introduced to verify the accuracy of horizontal slowness estimation; one to suppress aliasing effects due to possible secondary lobes of synthetic array beamforming calculated in horizontal slowness space and the other to reduce the event's mislocation caused by miscalculation of the horizontal slowness vector. Subsequently, a weighting technique is applied to combine the subfunctions into one single scalar objective function to use in the optimization process.

Key words: Array Seismology; Array design; Seismicity modelling.

1 INTRODUCTION

A seismic array consists of a number of sensors deployed in a special geometry with common precise timing, acquisition parameters and instrument type. Arrays have a variety of applications, particularly when the signal enhancement is a prerequisite to detect seismic events, and in situations where installing and maintaining sparse networks around the source is impractical. Study and monitoring of nuclear and chemical explosions (Baumgardt & Der 1998; Kim *et al.* 1998), volcanic and non-volcanic tremors (Saccorotti & Del Pezzo 2000; La Rocca *et al.* 2008; Ghosh *et al.* 2009), earthquake swarms (Hiemer *et al.* 2012) and real-time monitoring and early warning systems of active faults (Meng *et al.* 2014) are examples of array applications.

A remarkable utility of an array is to estimate the horizontal slowness vector of the incoming wave, which yields to phase identification and further seismological findings, such as event location and rupture front tracking (Krüger & Ohrnberger 2005; Ishii 2011). The accuracy of the array processing results relies on the coherency of the signal across the array. Coherency distortion may result from factors such as strong near surface heterogeneity, attenuation, strong local noise sources and radiation pattern of seismic waves. Near surface heterogeneities cause violation of the plane wave approximation that increases uncertainties of the estimated horizontal slownesses.

There are other sorts of uncertainties and aliasing in slowness vector estimation that are related to the array geometry. To eliminate them, some considerations in array configuration are commonly applied. For instances, each apparent wavelength of the signal under the study, λ_{app}, should be sampled in at least two discrete sampling locations so that the minimum interstation distance should be at least $\lambda_{app}/2$. In addition, to increase the resolution for the small wavenumbers, array aperture should be comparable with the highest apparent wavelength of the incoming signals.

Array geometry design has been systematically studied for seismic surface wave studies based on the array response function (ARF) characteristics (Wathelet *et al.* 2008; Marano *et al.* 2014). Kennett *et al.* (2015) suggested the use of spiral-arm shaped arrays,

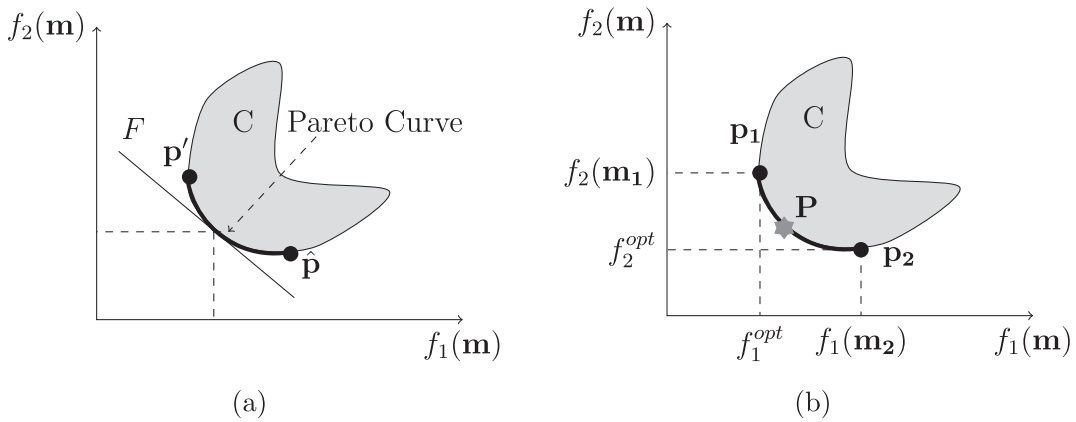

Figure 1. (a) Illustration of the Pareto curve for a 2-D objective function space. All points between $\mathbf{p}'$ and $\hat{\mathbf{p}}$ define the Pareto curve, the line F is a tangent to the curve at an arbitrary point and the region C is the feasible objective space. (b) Geometrical representation of the scalarization approach used to approximately define F as a weighted sum of the individual objective functions f_1 and f_2. Points $\mathbf{p_1}$ and $\mathbf{p_2}$ on the assumed Pareto curve are approximated by optimization of the single objective functions f_1 and f_2, respectively, and are used to define the weighting factor. The point $\mathbf{P}$ indicates a touching point on the Pareto curve that can be reached using the scalar objective function defined by the line F.

which allows deployment of relatively large aperture arrays with a limited number of stations to achieve a sharp central peak in the ARF and consequently a high slowness resolution. Haubrich (1968) investigated a special class of linear and planar arrays involving uniform patterns of stations, proposed a design method based on the co-array's properties and showed how the beam pattern can be optimized for a given number of sensors. However, idealized array configurations are difficult to realize in practice, especially on small scales, due to geographical and geological limitations.

The ARF depends on the relative position of array stations and the frequency content of the interesting signals, and for a specific frequency ω, it is defined as

$$\left| \frac{1}{N} \Sigma_{j=1}^{N} e^{2\pi i \omega (\mathbf{S}-\mathbf{S_0}).\mathbf{r}_j} \right|^2, \tag{1}$$

where $\mathbf{S} = (S_x, S_y)$ is the horizontal slowness vector, $\mathbf{S}_0$ is the correct horizontal slowness vector of the incoming waves, $\mathbf{r}_j = (\delta x_j, \delta y_j)$ is the horizontal location vector of the jth station relative to the array reference point and N is the number of stations (Rost & Thomas 2002; Schweitzer *et al.* 2012). In practice, the ARF is evaluated for a monochromatic wave with a fixed frequency, for exapmle, 1 Hz. Assuming the power spectral density (PSD) of the analysed waves is normalized to 1, then the ARF is considered to be equivalent of the total energy recorded by the array (Rost & Thomas 2002).

In many applications, information about deployment site and the experiment, such as site-specific noise level, properties of the target events, land-use classes (Büttner *et al.* 2004) and other constraints on the logistics are available. Such information needs to be integrated quantitatively to be used in the array geometry design and not just collected and qualitatively compared. For instance, to ensure high signal coherence and measure loss of signal across the array stations, it is advantageous to take focal properties of the target events and the site-specific noise level into consideration. However, considering such information is not standard, a quantitative integration method is required.

In this study, a flexible array design framework is introduced in order to perform an automatic search for an optimized array geometry considering additional information and constraints. This framework operates by modelling realistic conditions and scenarios and making use of synthetic seismograms to evaluate array beamforming as the design criteria instead of using the ARF (eq. 1). While the ARF is unique for a given array geometry regardless of seismological background and deployment site conditions, array synthetic beamforming is customizable for individual experiments. It is not straightforward to include station elevation differences in the ARF, but this can be achieved effortlessly using synthetic array beamforming. Although evaluating the ARF to design an array provides an effective criterion independent of further information such as velocity model and source properties, nevertheless, benefitting the realistic synthetic signals beamforming allows us to consider such a complementary information, which in some cases are vital to take into account, for example, loss of signal across array stations because of radiation pattern, existence of coherent noise and altitude deferences of array stations cannot be simply included in the ARF. In addition, the plane wave approximation is an implicit assumption while computing the ARF, whereas the time correction due to the deviation from the plane wave approximation at short source–receiver distances is easy to handle using realistic synthetic seismograms. Furthermore, the approach also allows to consider the joined effect of the newly created array and pre-existing network stations or arrays. One or more objective functions are defined depending on the purpose of the survey and specific boundary constraints. For instance, objective functions can ensure the precise slowness vector estimation of the earthquakes for a site-specific signal-to-noise ratio (SNR).

To describe the framework in detail, and to show how it works, we customized it with specified realistic constraints. The problem is to design a seven-station small-scale array to monitor earthquake swarm activity in the region of Northwest Bohemia/Vogtland. According to the survey goal, which is to obtain precise event locations derived by array method, two objective functions are defined. Then the weighting sum method is used to combine them in one scalar function. Both functions are used to control the accuracy of the horizontal slowness vectors of *P*- and *S*-phases estimated using the time domain beamforming of (noisy) seismograms from the hypothetic events in the target source region. One objective is to minimize the array beam power in a specified slowness range. The other one is to minimize the possible miscalculation of the main peak in horizontal slowness space. Details of the objective functions and the weighting technique are described in Section 2.

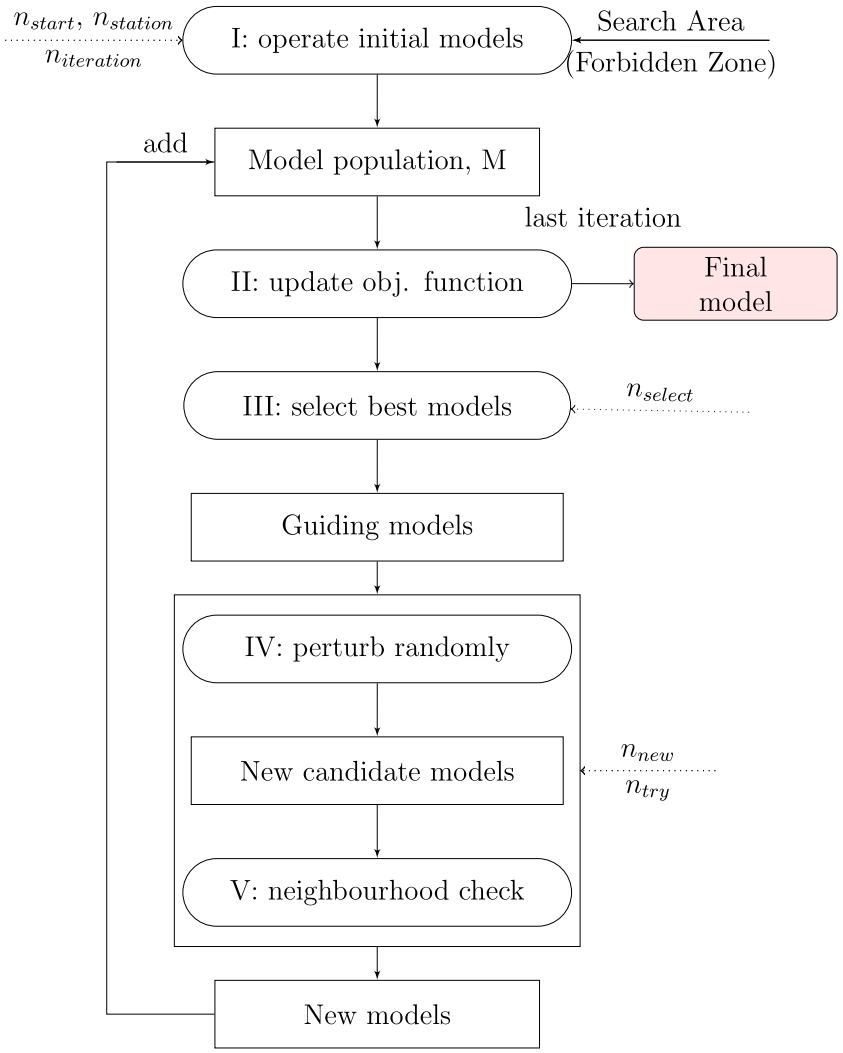

Figure 2. Optimization algorithm flowchart: the initial 'Model population, M' is created by drawing models from a given distribution, based on geometrical settings, the desired number of stations (n_{station}) and the number of initial models (n_{start}). $n_{\text{iteration}}$ is the number of iterations to create new models and to update M and the objective function population. n_{select} is the number of selected models from M with lowest value of the objective function used as 'Guiding models' to generate 'New candidate models' by random perturbations. n_{new} is the number of new models to be accepted in the neighbourhood of each of the n_{select} guiding models, n_{try} is the number of tries to find n_{new} accepted models to be added as 'New models' to M. After the last iteration, 'Final model' is the model in M yielding the lowest value in the objective function.

2 THEORETICAL APPROACH

We define a model as a specific geometrical configuration of the array for a given number of stations and specified deployment site, under optional boundary conditions as pre-existing stations. The model space covers all possible combinations of station positions. The aim is to find the best geometry, that is, a point in model space, at the minimum of a well-defined scalar objective function.

A key point of our approach is to solve the problem with the help of synthetic, full waveform seismograms. Although this is computationally demanding, it has the big advantage of flexibility when considering realistic source and site configurations and different types of noise. Additionally, user-specific processing schemes can be easily implemented and tested. We overcome the technical challenge of quickly calculating seismograms for many station-source configurations by means of pre-calculated Green's function databases and efficient storage and accessing tools (Heimann 2017).

To generate synthetic seismograms in the context of our scenario testing procedure, several pieces of information are needed: (1) a seismic source model including magnitude range, seismogenic zone and source mechanisms; (2) propagation velocity and attenuation model (if it is available), ideally with error bounds; (3) site specific characteristics such as noise level and amplification factors. Given a specific model has been generated during one iteration of the optimization process, the corresponding synthetic seismograms are recalculated for a given ensemble of seismic sources, and the scalar value of the objective function is calculated considering the complete ensemble of sources.

The random models are in principle drawn from a uniform distribution of virtual station points within the given boundaries of the deployment site. However, in order to consider constraints for the selection of sites, we work with 2-D probability density functions for selecting new models during each iteration. The probability density function may consider surface geology, boundaries of cities or countries, land use, accessibility as well as the natural and man-made sources of noise. For example, to avoid noisy station locations, land-use classes defined by the EU-project CORINE (Büttner *et al.*

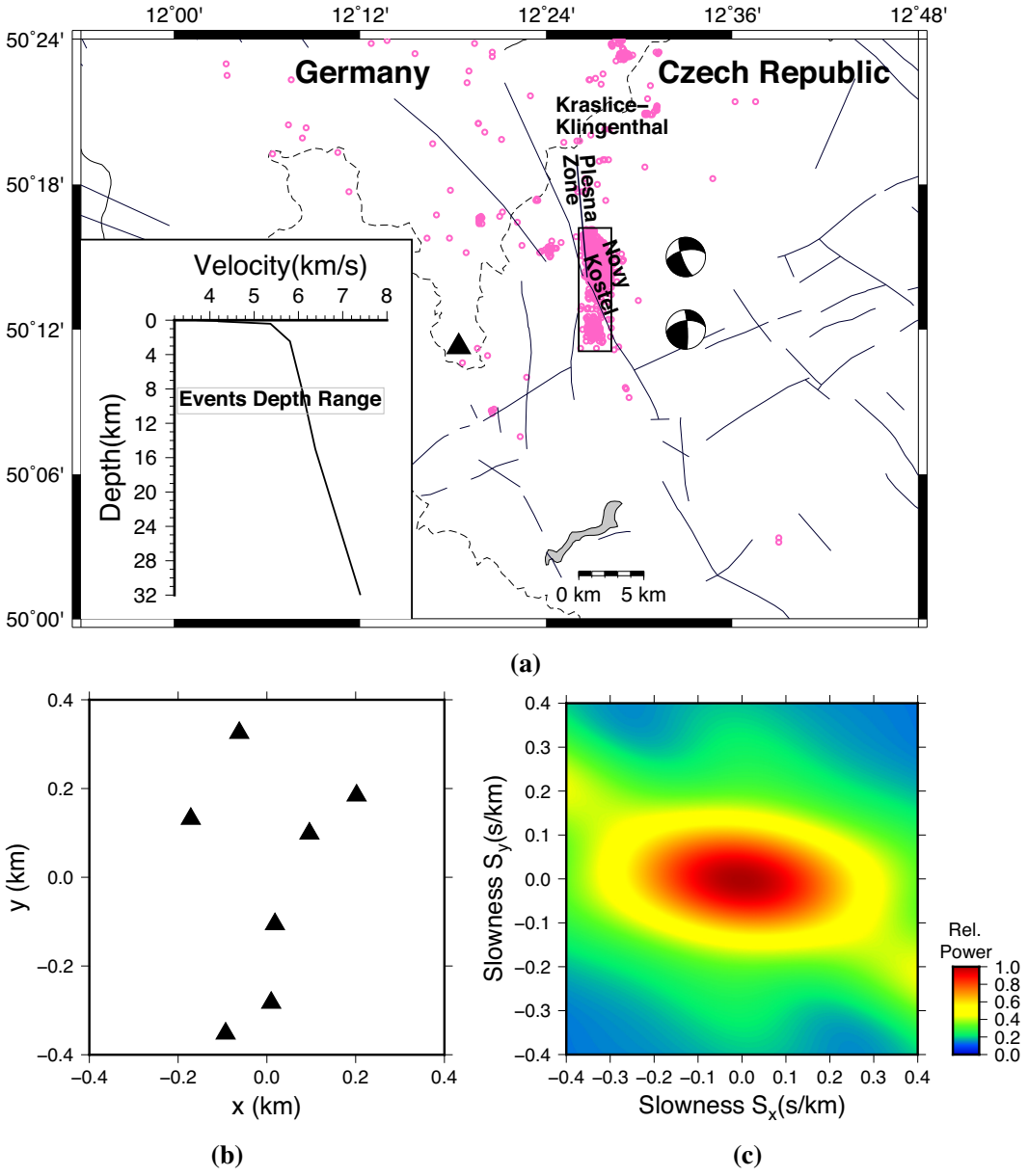

Figure 3. (a) Test area, which is an intraplate swarm region, pink circles are epicentres of earthquakes that occurred during 2013, the black triangle represents a temporary small aperture array, the Vogtland array, which operated from 2011 August 29 to 2011 November 2. The rectangle shows the Nový Kostel swarm zone, which we used as the target area. Two predominant focal mechanisms are shown. The inlay depicts the velocity model used to generate synthetic seismograms. (b) Geometry of the Vogtland array. (c) Array response function in slowness space.

2004) and open GIS data can be used to define such a 2-D probability density function. In the following subsections, we describe the selection of objective functions and the implemented search algorithm.

2.1 Objective functions and their scaling

As an example of application, we want to design a small aperture array for a given number of stations to detect, absolutely locate and map the migration pattern of clustered, weak events of earthquake swarms or aftershock activity. Therefore, the aim is to ensure a high resolution of the horizontal slowness vectors estimation of *P*- and *S*-phases for individual events occurring within a confined source volume with given, predominant mechanism and magnitudes. In this example, we define two objective functions using time domain beamforming of *P*- and *S*-phases in the (noisy) seismograms from hypothetic events in the target source region to verify the accuracy of horizontal slowness estimation, without using the idealized concept of ARFs. We measure the total amount of relative power of array beam in slowness space, for a given source and array geometry that ideally should contain a concentrated main peak and no other localized secondary peak. The array beam trace is calculated as the sum of all recorded, time shifted traces:

$$B(t) = \frac{1}{n}\Sigma_{j=1}^{n}\ Y_j(t + \mathrm{d}T_j) \quad \text{with} \quad \mathrm{d}T_j = S_x\delta x_j + S_y\delta y_j. \qquad (2)$$

where Y_j is the normalized trace recorded at the station j and n is the number of stations. Assuming the plane wave approximation is valid, the time shift, $\mathrm{d}T_j$, for the station j, depends on the horizontal

Table 1. Input parameters used in the scenario modelling for swarm monitoring in Northwest Bohemia/Vogtland.

Parameter	Value
Velocity model	1-D model based on Málek *et al.* (2004)
Noise level (PSD)	Calculated from recorded noise samples
Focal mechanisms	(1) Oblique-normal; strike: 160° ± 5°; dip: 75° ± 5°; rake:−30° ± 10° (2) Oblique-thrust; strike: 357° ± 5°; dip: 83° ± 5°; rake: 37° ± 5°
Fault plane	Nový Kostel fault geometry; strike: 169°, dip: 80°
Hypocentral distribution	Fault plane ± 0.1 km
Sampling rate	originally 100 sps, upsampled to 400
Magnitude	M_w: 1
Frequency band	2–8 Hz
Slowness range	±0.3 s km^{-1} for both *P*- and *S*-phase
Number of slowness grids	200
Number of simulated events	100

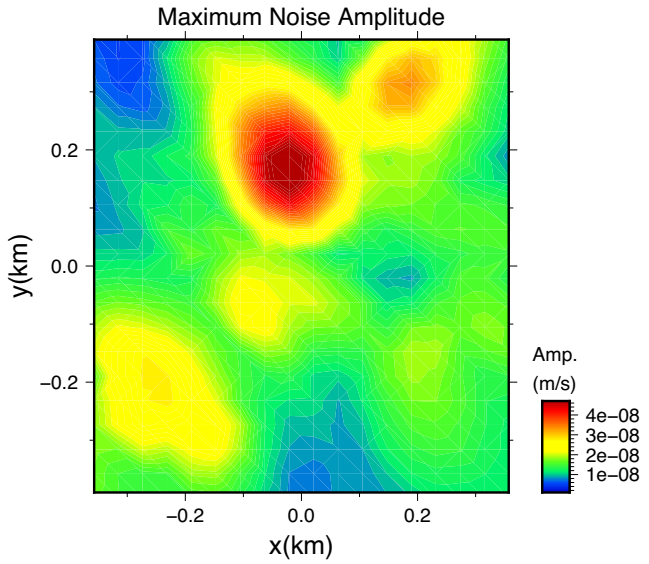

Figure 4. Simulated noise signal amplitude by assuming a cluster of point sources and explosion sources at the surface of the deployment site.

slowness components of the incoming wave front, S_x and S_y, and the relative distance to the array reference point, δx_j and δy_j. We assumed that there is not any overlap of phases in the processing time window, so that using the normalized traces eliminates the effect of radiation pattern on amplitudes. A common strategy to find the correct value of time shifts is described in, for example, Schweitzer *et al.* (2012) and Rost & Thomas (2002). $B(t)$ is calculated for an appropriate time window of *P*- and *S*-phases.

The first objective function, f_1, is defined by assuming that the average relative beam power of the *P*- and *S*-phases in the slowness space is minimal. For *P*-phase that is calculated by

$$f_p = \frac{1}{n_x n_y} \Sigma_k^{n_y} \Sigma_l^{n_x} A^2_{S_{x_l}, S_{y_k}}, \tag{3}$$

where n_x and n_y are the number of grid points in the pre-defined slowness ranges S_x and S_y, index p of f_p indicates the *P*-phase and A^2 is the value of beam power, which is normalized to the global maximum of all tested gridpoints, so it is called relative beam power. In the same way, the average relative beam power for the *S*-phase is written as f_s, and finally both phases are combined in a single formula:

$$f_b = \sqrt{{f_p}^2 + {f_s}^2}. \tag{4}$$

f_b is calculated using synthetic waveforms of a given specific source from the ensemble of target sources and can also be calculated from the whole ensemble to include a realistic model of seismicity, leading to f_1 defined by

$$f_1 = \frac{1}{n} \Sigma^n f_b, \tag{5}$$

where n is the number of events. A larger value of f_1, indicates higher value of average beam power in the slowness space for the whole set of earthquakes, which can happen either because of high or numerous side lobes or a wide main lobe in the slowness map, for a number of individual earthquakes, both of which are undesirable.

The second objective function, f_2, is defined to minimize the possible miscalculation of the horizontal slowness vector, that is, the main peak in the horizontal slowness space. Such a misplaced beam power peak in the slowness space can occur, if for instance the wave front is affected by a nodal plane of the source radiation pattern, if the waveform becomes non-coherent close to the nodal plane and if the plane wave approximation is not valid. Other causes may be related to the heterogeneous distribution of ambient noise or noise sources across the array, or if local site effects and amplification factors distort the waveform coherency. Nevertheless, modelling 3-D propagation effects such as lateral heterogeneities is hard to realize before the experiment, and in practice, the measurement bias of the horizontal slowness vector due to such incoherent sources is usually corrected by employing station azimuthal correction terms during the operation of an array (Bondár *et al.* 1999). In our modelling, we try to minimize errors caused by source radiation pattern and local site conditions such as the noise level.

A miscalculation of slowness vector would lead to an error in the location of the earthquake source, that is, a deviation between calculated and true event location. We prefer to include mislocation in the objective function rather than the miscalculation of slowness because mislocation is a quantity that can be shared between array and network processing if network stations are included. We implement a location procedure that relies on ray tracing of *P*- and *S*-phases given the measured slowness values and the velocity model of the propagation media. We use a common layered model in our example, but it would be possible to consider local site effect models for every station. A unique ray geometry, $R(X, Z)$, and travetime function of ray position, $X(t)$ and $Z(t)$, are determined for both the *P*- and *S*-phases. $X(t)$ and $Z(t)$ are time sequences of distance from the source and depth, respectively. Since the aim is to calculate the location error caused by miscalculation of slowness, we employed theoretical phase arrival times using the velocity model and source location without assuming any uncertainty. Epicentral distance and

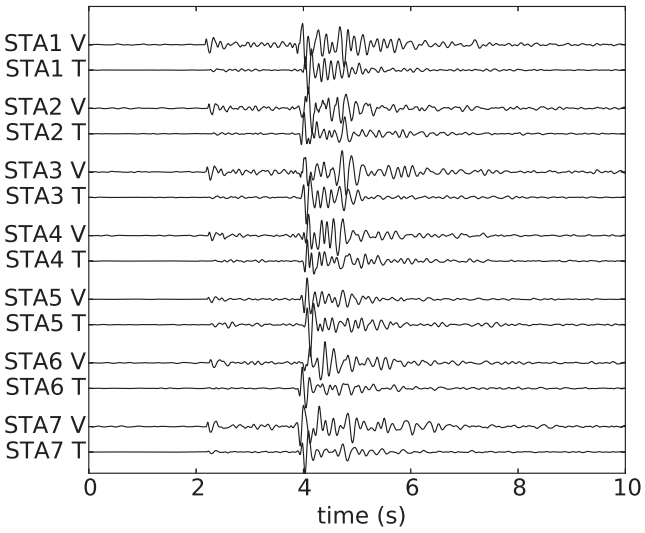

(a) Real waveforms.

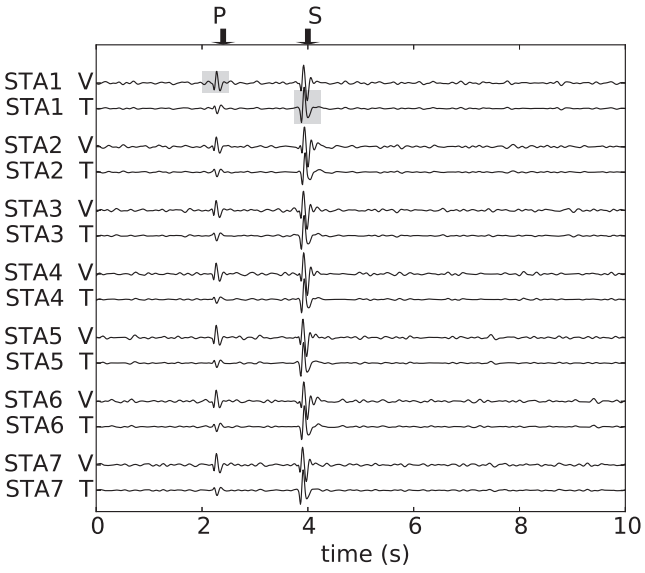

(b) Synthetic waveforms.

Figure 5. An example of real and synthetic waveforms recorded on vertical (V) and transverse (T) components. (a) Real signals recorded at the seven-station Vogtland array shown in Fig. 3(b), magnitude of the event is *Ml* = 0.9 and is located in the Nový Kostel zone. Traces are normalized to 1, bandpass filtered 2–8 Hz. (b) Synthetic waveforms after adding realistic noise and bandpass filtered 2–8 Hz. *P*-phase analysis is done on the phase window on V, to estimate slowness and backazimuth angle, then horizontal components are rotated according to the backazimuth and the T components are computed. The *S*-phase processing is done on the phase window on T.

depth are then estimated from the crossing point of *P*- and *S*-phase ray trajectory, given the arrival times. First, using arrival time differences, epicentral distance is calculated. Then, corresponding depth, z is derived from the average value of Z(t) for the *P*- and *S*-phases. Together with the backazimuth angle estimated from the horizontal slowness vector of the *P*-phase, the latitude and longitude of the epicentre are determined. Horizontal mislocation, δ_h, and depth error, δ_d, are obtained by comparing calculated and true location. The

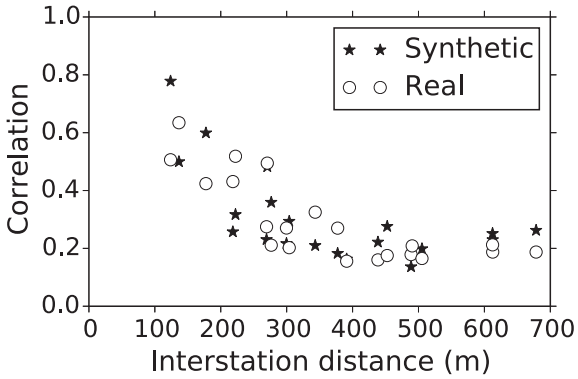

Figure 6. Cross-correlation of real (circles) and synthetic (stars) noise samples for the seven-station Vogtland array shown in Fig. 3(b).

total mislocation is defined by

$$f_l = \sqrt{\delta_h^2 + \delta_d^2}. \tag{6}$$

After calculating f_l for n events of ensemble of target events, the average value of total mislocations is defined as the second objective function, f_2, by

$$f_2 = \frac{1}{n}\Sigma^n f_l. \tag{7}$$

Having defined two objective functions, we use a weighting technique to combine them into one scalar function. In general one can customize the problem by defining any number of objective functions, so we describe the weighting technique in a general form.

A multi-objective optimization problem is defined in mathematical terms as

$$\min\,[f_n(\mathbf{m})]; \quad \mathbf{m} \in S, \tag{8}$$

where $f_n(\mathbf{m})$ is a set of objective functions with n member, $\mathbf{m}$ is a vector of design variables and S is a feasible search region defined by a set of constraints. Single objective optimization is formulated by $n = 1$. Without loss of generality, the number of objective functions in our problem is $n = 2$, and f_1 and f_2 are the two independent objective functions for two criteria defined in eqs (5) and (7).

Contrary to a single objective problem, a solution to a multi-objective problem is not a single global solution, and it is required to specify a set of solutions that all satisfy a predetermined definition of optimum solution (Marler & Arora 2004). 'Optimal' solution for the non-unique multi-objective optimization is defined using the concept of the 'Pareto optimality' (Laponce 1972; Marler & Arora 2004). A vector $\mathbf{m}^* \in S$ is named Pareto optimal if all other vectors $\mathbf{m} \in S$ have higher values for at least one objective function, or have the same value for all the objective functions (Laponce 1972; Marler & Arora 2004; Caramia & Dell' Olmo 2008). Let's assume a region, C in Fig. 1, in the 2-D objective function space, $f_1 - f_2$, is covered by feasible values of functions f_1 and f_2 for all possible models $\mathbf{m} \in S$. All points between $\mathbf{p}'$ and $\hat{\mathbf{p}}$, indicated by the thick line on Fig. 1(a), define the Pareto curve or Pareto front that is the image of all the Pareto optimal solutions in the objective function space. The shape of the Pareto curve indicates the nature of the trade-off between the different objective functions, and there is mathematically no better solution for the optimization problem than any point on the Pareto curve. Finding the Pareto curve from random sampling in the model space is computationally often not possible, so approximation methods are frequently used (Caramia & Dell' Olmo 2008). In our example of a 2-D objective space, the final objective function can

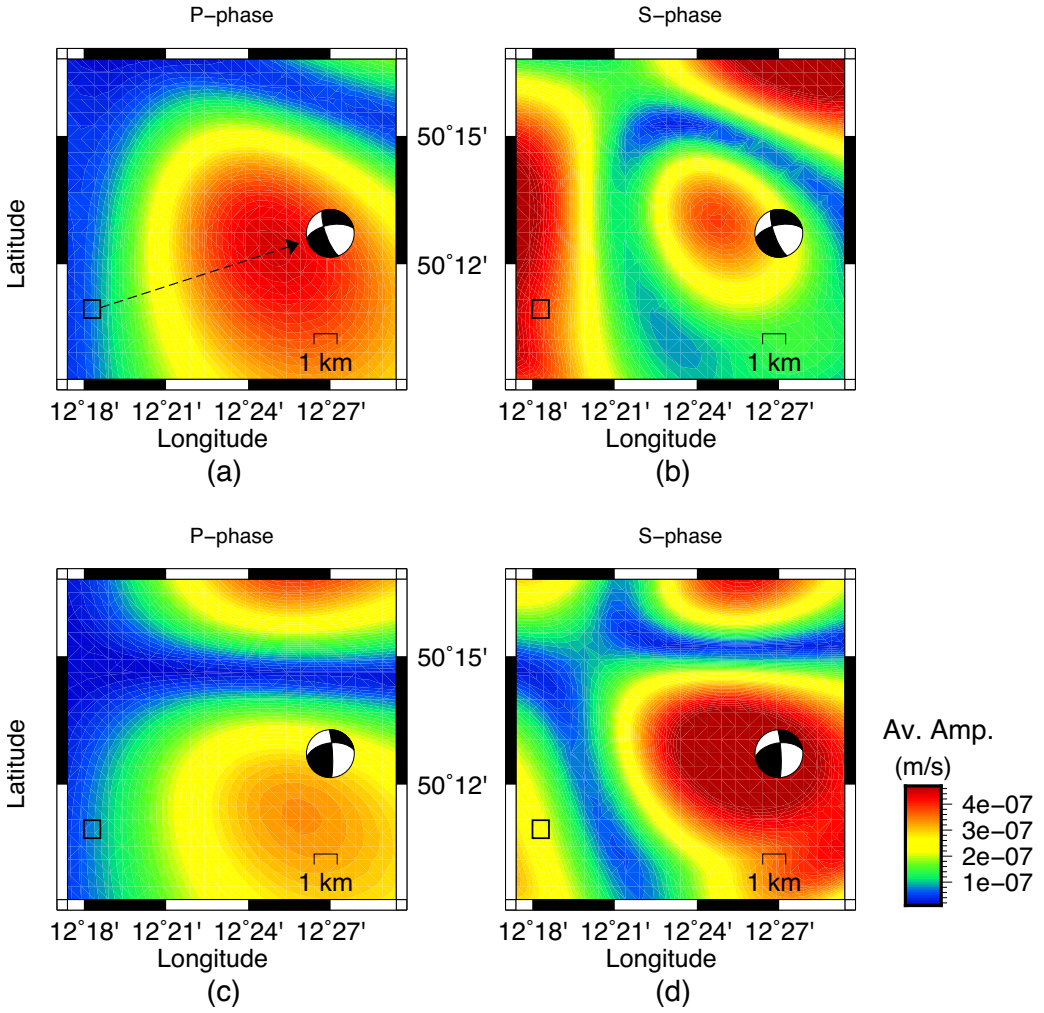

Figure 7. Radiation pattern of body waves for two types of events characteristic of the seismicity of the target area. Panels (a) and (b) show the average value of *P*- and *S*-phase amplitudes for oblique-normal events and panels (c) and (d) show the average value of *P*- and *S*-phase amplitudes for oblique-thrust events. The small area shown by the rectangle is the area where the array is supposed to be deployed and the arrow on plot (a) indicates the backazimuth direction to the target events.

be written as a line (dimensionless) tangent to the Pareto curve:

$$F = \gamma f_1(\mathbf{m}) + (1-\gamma) f_2(\mathbf{m}), \tag{9}$$

where γ $(0 \leq \gamma \leq 1)$ is a weighting or normalization factor between f_1 and f_2. Obviously, changing the weight γ leads to possibly different touching points of F (Fig. 1a). There is not a deterministic correspondence between the weighting factor and the solution of the optimization, so the user should determine the appropriate weight. However, the weighting factor does not necessarily correspond directly to the relative importance of the objective functions (Caramia & Dell' Olmo 2008).

Eq. (9) can be rewritten as

$$f_2(\mathbf{m}) = \frac{-\gamma f_1(\mathbf{m})}{1-\gamma} + \frac{F}{1-\gamma}. \tag{10}$$

So, the minimization in the scalarization approach can be interpreted as the attempt to find the touching point for a tangent with slope $-\frac{\gamma}{1-\gamma}$ (Fig. 1a). By determining γ, F is formulated as a joint scalar objective function, which can lead the optimization process to one Pareto optimal solution, for example, point P on Fig. 1(b). Our strategy to estimate γ is to use points $\mathbf{p}_1$ and $\mathbf{p}_2$ (Fig. 1b) to estimate the slope in eq. (10). We assume that $\mathbf{p}_1$ and $\mathbf{p}_2$ represent the optimized solution of individual objective functions f_1 and f_2, respectively. Accordingly, the optimized models, $\mathbf{m}_1$ and $\mathbf{m}_2$, and related minimum values, $f_1(\mathbf{m}_1)$ and $f_2(\mathbf{m}_2)$ are obtained through the optimization process. The associated values of $f_2(\mathbf{m}_1)$ and $f_1(\mathbf{m}_2)$ are obtained by simple forward simulation. Finally, the slope of an assumed passing line from $\mathbf{m}_1$ and $\mathbf{m}_2$ is calculated and the value of γ is estimated from $-\frac{\gamma}{1-\gamma}$. Knowing γ the final solution can be obtained by minimizing F for the joint problem.

In general, the procedure is extendible for any number of objective functions. For instance if $n = 3$, two normalization factors γ_1 and γ_2 are used to modify eq. (9).

2.2 Optimization method

The aim is to search for an array geometry that, given a set of synthetic events, gives the best array performance according to the scalar objective function described in Section 2.1. For a similar problem of optimized network design, Hardt & Scherbaum (1994) applied a simulated annealing (SA) technique. The SA algorithm operates by sequence of steps, controlled by a pre-defined cooling

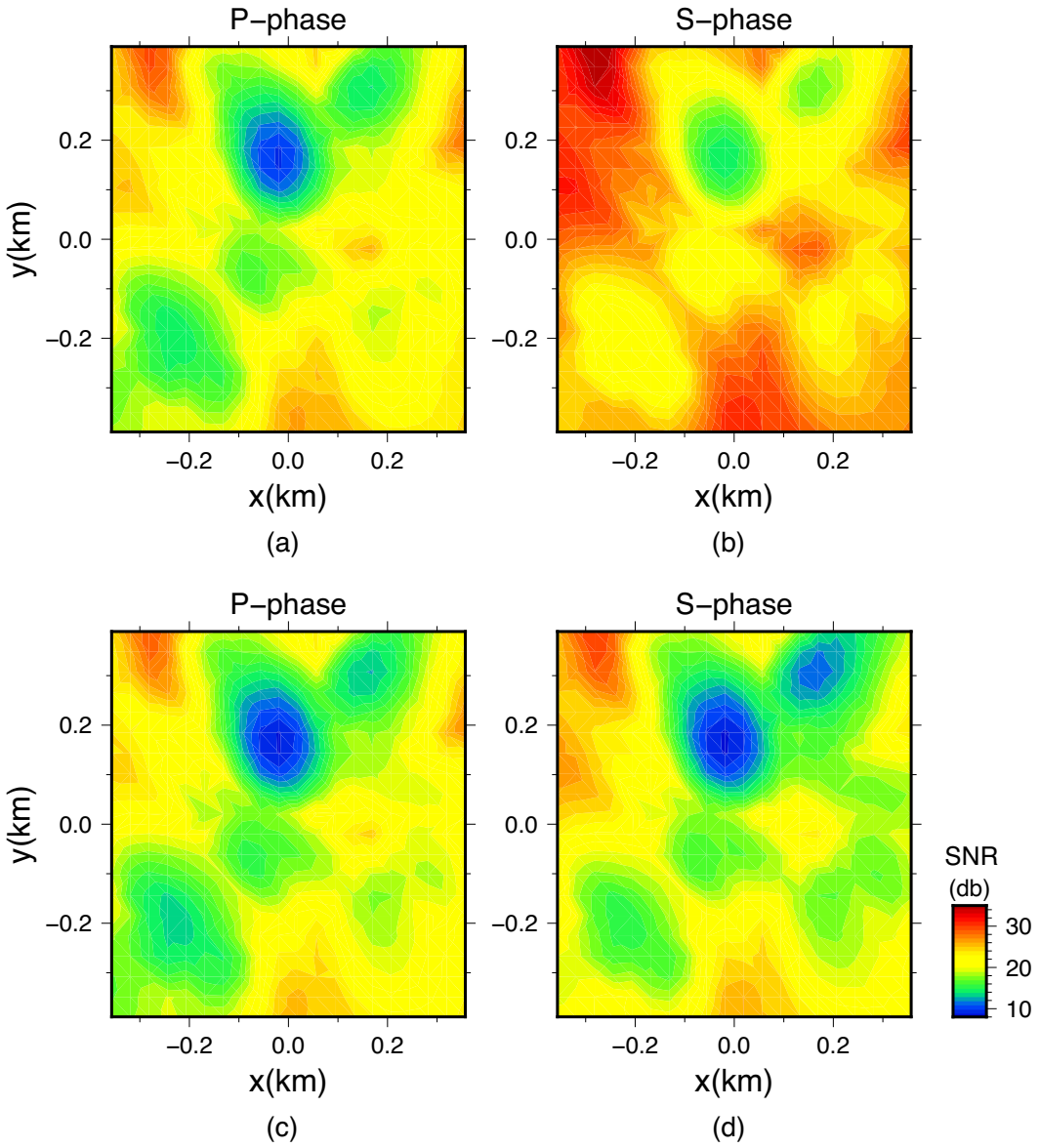

Figure 8. Average SNR of *P*- and *S*-phases for the synthetic events modelled in the Vogtland area (small rectangle in Fig. 7). The noise model is shown in Fig. 4 and signal amplitudes are shown in Fig. 7. Panels (a) and (b) are related to the oblique-normal events and panels (c) and (d) are related to the oblique-thrust events.

Table 2. Input parameters used to set up the optimization algorithm.

Parameter	$n_{station}$	$n_{iteration}$	n_{start}	n_{select} †	n_{new}	n_{try}
Value	7	12	500	50; 40; 30; 25; 25; 20; 20; 10; 10; 10; 10; 10	15	5

† Values of n_{select} are specified for each iteration.

scheme, and starts with an initial model estimation and the objective function evaluation. The next steps are new model generation by perturbation of a given model and making decision about the acceptance or rejection of that model based on specified criteria (Sen & Stoffa 2013). The main drawback of the SA technique is the large number of function evaluations needed to generate converged statistics. For instance, Hardt & Scherbaum (1994), suggested a cooling scheme based on which 14×10^5 function evaluations are needed to find an optimum configuration for a seven-station network. The objective function calculation in our approach is computationally expensive as it takes about 2.5 min for one function evaluation using an eight-core processor. Thus we tried to modify the SA procedure so that it converges to a minimum value in less number of evaluations. Accordingly, we benefit from a sampling technique based on the neighbourhood concept (Sambridge 1999; Wathelet 2008) and objective function approximation using Voronoi cells (Okabe *et al.* 1992).

A model is determined by the position vectors of the array, while the array stations are ordered based on the distance from the lower left corner of the deployment site. The outline of the algorithm

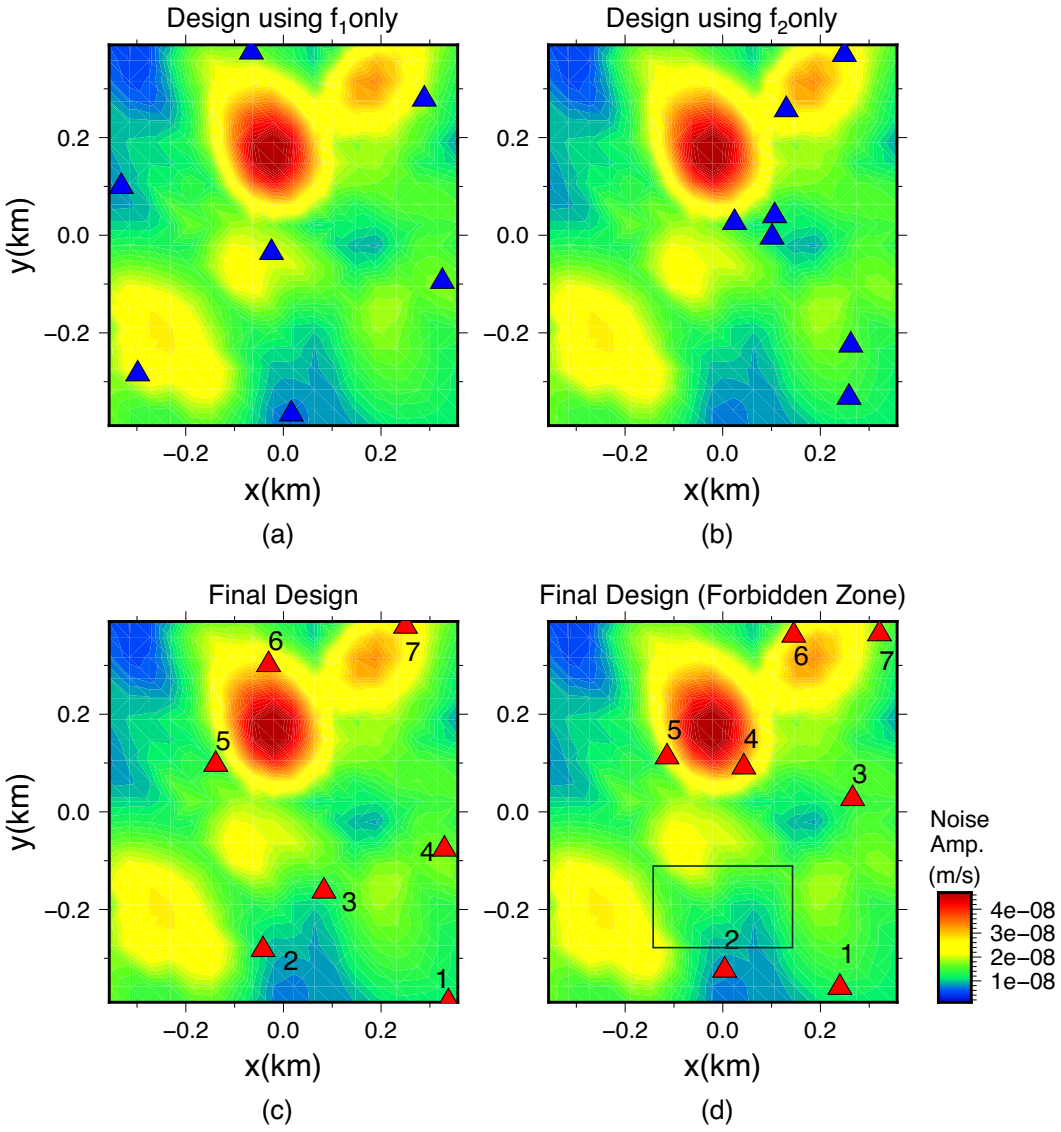

Figure 9. Optimized geometries found by using (a) f_1 (array beam power) and (b) f_2 (precise slowness vector) as objective function. Corresponding values of the objective functions are used to estimate γ in eq. (10). (c) Final optimized geometry suggested for the test area using the final combined objective function (eq. 12). (d) The geometry suggested assuming an extra condition that is a forbidden zone in the area is indicated by a black rectangle. The simulated noise amplitude pattern is depicted in the background of all figures. The related co-arrays and ARFs are plotted in Figs 12 and 13, respectively. In plots (c) and (d), station numbers are corresponded to the histograms depicted in Figs 11 and 16, respectively, which indicate potential adjustments of each station calculated from the family of solutions.

is shown in the flowchart in Fig. 2 and works according to the following steps:

(1) A number of initial models, n_{start}, with known number of stations, n_{station}, are randomly drawn from a given distribution defined based on the search area and possible one or more forbidden zones, so the model population, M, is generated. (2) For every element of the model population, $\mathbf{m_j}$, a forward calculation is done, so the objective function population, $F(\mathbf{m})$, is created. (3) In every iteration, a number of n_{select} models with lower value of $F(\mathbf{m})$ are chosen from the model population as guiding models. (4) New models are generated by random perturbation of the guiding models so an ensemble of candidate models, $n_{\text{candidate}}$ models, is created. The radius of random perturbation is reduced by increasing the iteration steps using a cooling scheme. (5) The neighbourhood check is done to determine if the candidate models fall into the same Voronoi cell as the corresponding guiding model or not. n_{new}($< n_{\text{candidate}}$) models are accepted from each ensemble and are added to the model population. If in the first try n_{new} models are not found for a guiding model, this step is repeated several times until n_{new} models are found, but the number of tries are limited to n_{try}.

In every iteration, new accepted models are added to the M and $F(\mathbf{m})$ is updated. So the iteration is done over steps (2) to (5). After the last iteration, the model with lowest $F(\mathbf{m})$ is reported as the final model.

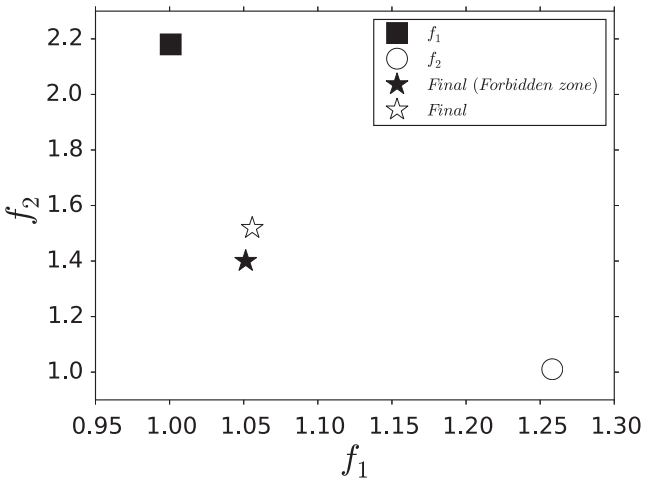

Figure 10. The value of subfunctions for the geometries introduced in Fig. 9. The square and the circle represent geometries that are outcomes of a single objective optimization using f_1 and f_2 individually to approximate the Pareto curve and to estimate the coefficient γ in eq. (9). The white star represents the final optimized model and the black star corresponds to the optimized geometry under the additional constraint of a forbidden zone in the search area; both solutions are obtained from the minimum value of the objective function.

3 APPLICATION TO DESIGN OF A MONITORING ARRAY FOR MID-CRUSTAL EARTHQUAKE SWARMS

3.1 Model set-up

The target area, Northwest Bohemia/Vogtland, is one of the most active intraplate earthquake swarm regions in Europe. It is situated in the border region between Germany and the Czech Republic. In 2010 for 6 months, a seismic array of seven stations was installed, by University of Potsdam, near the German–Czech border to monitor swarm activities. Position of the array is shown by a black triangle in Fig. 3(a), and array geometry and the ARF are depicted in Figs 3(b) and (c), respectively.

Earthquake swarms encompass an immense number of weak events occurring in a spatio-temporal cluster over a period of weeks or months, and are not associated with typical mainshock–aftershock sequences of an earthquake. They are considered to result either from magmatic activity (Morita *et al.* 2006; Dahm *et al.* 2008), from fluid migration (Hensch *et al.* 2008; Hainzl *et al.* 2016) or from aseismic creep on faults (Neunhöfer & Hemmann 2005; Passarelli *et al.* 2015). Seismic swarms in Northwest Bohemia/Vogtland often comprise more than 10^3–10^4 individual events with magnitudes between $M1$ and $M4$ (Růzek & Horálek 2013). Typically, the events are clustered in several focal zones (Nový Kostel, Kraslice–Klingenthal, Plesna, etc.) and the hypocentral depths of events in the whole region vary between 5 and 20 km (Růzek & Horálek 2013). However, during the last 25 yr, most of the seismic activity took place near the village of Nový Kostel, where the hypocentres are located in a depth range between 7 and 10 km (Růzek & Horálek 2013). The Nový Kostel zone shows a fault plane at depths between 6 and 11 km oriented nearly S–N (strike 169°) and steeply dipping (dip 80°) westwards. The epicentres of earthquake swarms that occurred between 1991 and 2001 and in 2008, are distributed along the 12.5 km long section of the fault line (Fischer & Horálek 2003; Fischer *et al.* 2010).

According to Horálek & Šílený (2013), the focal mechanisms of the swarm activity that occurred close to Nový Kostel in 2000 are mostly oblique-normal and oblique-thrust but the oblique-normal faulting predominates. The mechanisms of the individual types are fairly consistent, where the oblique-normal events have predominant strikes of 160°–170°, dips of 72°–80° and rakes of −28° to −38°, whereas the oblique-thrust events show mainly strikes of 355°–360°, dips of 80°–85° and rakes of 35°–40°. This area has been of a great interest for seismologists and has been studied for different subjects such as location of hypocentres (Fischer *et al.* 2010; Hiemer *et al.* 2012), magnitude estimation (Horálek *et al.* 2009), determination of focal mechanisms (Dahm *et al.* 2000; Horálek & Šílený 2013) and determination of optimum velocity models (Málek *et al.* 2004, 2005). In this region during a swarm event in 2008, a seismic array helped in the detection of small magnitude events (Hiemer *et al.* 2012) and the region is also selected for developing an interdisciplinary observatory using shallow drilling and small aperture seismic arrays (Larsen 2012).

We use this region as an example and ask the question of how the design of a temporary array installation could be improved by rearranging its stations. However, by presenting this example the aim is to show how the array design framework can be customized given a specific problem.

3.2 Simulating synthetic waveforms

The essential information needed to set up the array design framework and to simulate synthetic waveforms are summarized in Table 1. The velocity model that is used to generate synthetic signals as well as to predict phase arrival times is based on Málek *et al.* (2004; see Fig. 3a).

100 simulated events are assumed to be distributed uniformly within 100 m bands around the main fault plane near Nový Kostel. Consequently, the depth of events are between 8 and 11 km. The source mechanism of each particular event is assigned randomly from valid ranges of strike, rake and dip values of oblique-normal and oblique-thrust type events (50 mechanisms of each type, see Table 1 for valid ranges). We decided to use magnitude M_w1 for all of the simulated events, so the variation of SNR in the analysed signals results from the change in noise amplitude and signal amplitude due to the radiation pattern.

To simulate realistic background noise traces, noise PSD is calculated using real samples recorded by the array that was operated in the same zone (Fig. 3a). In reality, noise PSD can vary depending on the measurement location even in 1 km distances, due to localized noise sources. Localized noise sources are modelled by assuming a cluster of point sources and explosion sources with random mechanisms, origin times and locations at the surface of the search area. Accordingly, a stochastic three-component noise trace is produced that can be tuned to have the same PSD level as that calculated from real samples. In this way, synthetic noise samples show realistic variation in PSD in different random stations, while properties of the noise signals such as high degree of coherency at short distances and within three components are simulated realistically. Fig. 4 illustrates a distribution of noise amplitude that are simulated by the noise generator used in this study.

Examples of real and synthetic waveforms are shown in Fig. 5 where the array geometry was introduced in Fig. 3. Fig. 6 shows noise signal spatial correlation derived from 10 s duration samples of real and simulated noise. For both cases array station locations are the same. Comparing the overall trends of synthetic and real noise

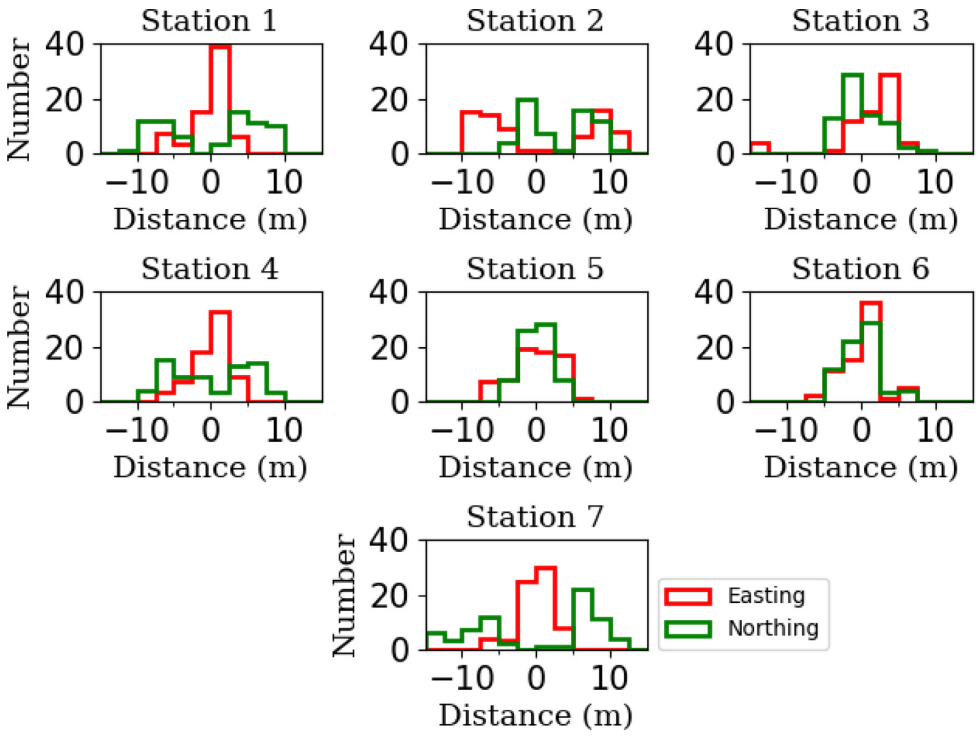

Figure 11. Histograms of the spatial distribution of family of solutions for the geometry shown in Fig. 9(c). For each station the red line shows the distribution of distances in east–west direction relative to the average location and the green line illustrates the same values in the north–south direction. Station numbers are in agreement with the station order in Fig. 9(c).

data indicates that the distance-dependent coherency of synthetic noise signals is realistic.

Fig. 7 shows average radiation pattern of *P*- and *S*-phases for simulated events in an area including the search box (black rectangle). The oblique-normal and oblique-thrust events are analysed separately, and the main focal mechanisms are shown in the location of assumed sources. These plots show that within the small search area, signal amplitudes vary slightly. According to Figs 7(a) and (c) *P*-phases average amplitudes are in the same range for both type of events, while the amplitude of *S*-phases are higher for oblique-normal events (Fig. 7b) compared to the oblique-trust events (Fig. 7c). Using the noise model illustrated in Fig. 4, the average SNR for phases recorded at the deployment site is calculated (Fig. 8). We express the SNR in decibel as

$$\mathrm{SNR} = 10 \log_{10} \frac{P_\mathrm{S}}{P_\mathrm{N}}, \tag{11}$$

where P_S is the power of the signal, *P*- or *S*-phase wave, and P_N is the power of the noise. P_S and P_N are computed in the time domain as an average power over the duration of 1 s.

All synthetic traces are filtered before beamforming using the bandpass Butterworth filter of order 4 and corner frequencies of 2 and 8 Hz. According to the velocity model and the hypocentral distribution of events, realistic slowness ranges for *P*- and *S*-phases are about 0.12–0.16 and 0.17–0.24 s km^{-1}, respectively. Thus, the wavelength (λ) range of the waves, 0.5–4 km, is much smaller than the distance travelled by the wave front, $r \approx 13$ km, and the plane wave approximation condition, $r \gg \frac{\lambda}{2\pi}$ (Ben-Menahem & Beydoun 1985), is valid. The highest value for the slowness is set to 0.3 s km^{-1} for both phases, and the number of gridpoints for each slowness component, that is, n_x and n_y, is equal to 200. Required parameters to set up the optimization algorithm are summarized in Table 2.

3.3 Results and discussions

3.3.1 Estimation of weighting factor: γ

To estimate the weighting factor in eq. (10), according to the procedure described in Section 2.1, the optimization program is initiated using each objective function f_1 (eq. 5) and f_2 (eq. 7) individually. For each case the same scenario and boundary conditions are applied that are described in detail in Section 3.1. The optimized models for each objective function are shown in Figs 9(a) and (b), where the assumed noise maximum amplitude distribution is depicted in the background. The values of the two objective functions for the geometry shown in Fig. 9(a) are $f_1 = 1.0$ and $f_2 = 2.18$, and for the geometry shown in Fig. 9(b) are $f_1 = 1.26$ and $f_2 = 1.0$, and are marked in Fig. 10 by a circle and filled square, respectively. By substituting those values in eq. (10), γ is calculated equal to 0.88. Accordingly, the final scalar objective function is

$$F = 0.88 f_1 + 0.12 f_2. \tag{12}$$

3.3.2 Optimized array

In the ideal case, the final objective function should lead to a solution that minimizes both functions f_1 and f_2 simultaneously. However, in practice there might be an inherent trade-off between the two functions, and such an ideal solution might not exist. In general, the actual shape of the Pareto front is unknown in this problem. Using the final objective function (eq. 12), which is a weighted sum of f_1 and f_2, we try to get as close as possible to an ideal solution.

The minimum value of the final objective function gives the solution, which is shown in Fig. 9(c), and the corresponding values of the individual objective functions $f_1 = 1.05$ and $f_2 = 1.4$ are shown in Fig. 10 by a white star. To allow for small variations in

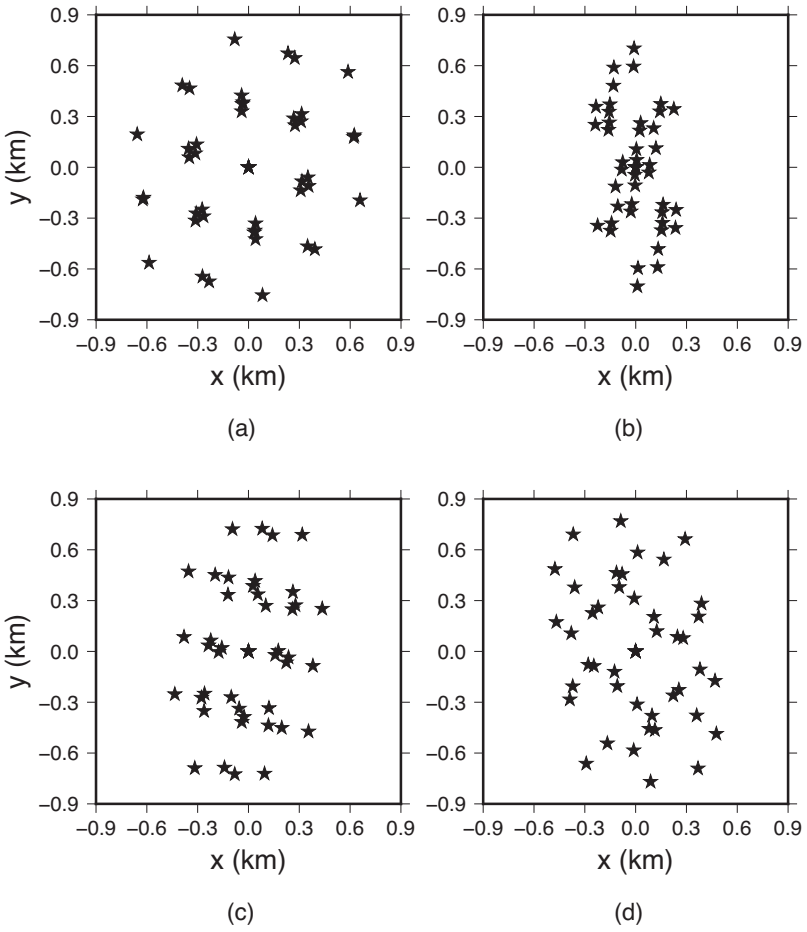

Figure 12. Co-arrays of the arrays shown in Fig. 9.

each station location to take into account unforeseen restrictions in the field, we suggest to consider the family of best solutions as well. The family of solutions is determined by applying a threshold on the final objective function. For instance, for the solution shown in Fig. 9(c), the minimum of the objective function augmented by a factor of 0.02 is assumed as threshold value. Accordingly, the spatial distribution of all models whose objective functions fall below the threshold, gives an indication for possible adjustments of the final deployment, while for each station, the average location of the clustered solutions reveals an alternative station location. Fig. 11 shows the family of solutions in terms of histograms of the relative distances of the stations that are measured in east–west (red) and north–south (green) direction from the average model, where the station numbers correspond to the numbers shown in Fig. 9(c).

A comparison between the three solutions, shown in Figs 9(a)–(c), is performed by evaluating the co-array of each array geometry, which illustrates the set of all interstation distances. (Haubrich 1968). According to the co-arrays depicted in Fig. 12, it is obvious that the objective function that is related to the array beam power, that is, f_1, has a tendency to distribute stations regularly with large interstation distances, such that the smallest interstation distance for the related optimized model (Fig. 9a) is bigger than those in the other two arrays. In addition, the maximum interstation distance for this case is comparable with the dimension of the deployment site. On the other hand, the objective function f_2, which is related to the precision of the slowness vector, results in a model (Fig. 9b) that has stations at closer interstation distances to achieve a better azimuthal resolution of the target swarm area (the backazimuth to the swarm region is shown in Fig. 7a). Nevertheless, the final optimized solution (Fig. 9c) keeps properties of two other models as much as possible to achieve optimization in terms of both desired properties measured by the contributing functions.

In all cases, the optimization algorithm avoids the high-noise area (red colours in Fig. 9) for deployment of any station, although to achieve optimal interstation distances and optimal azimuthal resolution, some stations are selected at the margin of the high-noise area (yellow colours in Fig. 9). Although the ARF has not been considered directly as a design criteria, it can be used to compare the array geometries as a standard tool, so the ARFs of the models are plotted in Fig. 13. A circular shape of the ARF's main lobe in Fig. 13(a) reflects a uniform distribution and azimuthal symmetry of the related interstation distance vectors (Figs 9a and 12a), while non-uniform distribution of the other two geometries (see Figs 9b and c and Figs 12b and c) causes the elliptical main lobes with the minor axes, that is, highest array resolution, in the azimuthal direction of the events.

Convergence rate of the final objective function is shown in Fig. 14. According to the initial set-up parameters (Table 2), the first 500 models are randomly chosen, while the later models are generated by perturbing the selected guiding models to reduce the value of the objective function. A relatively large variation in the early iterations is due to the large dimension of the explored model space,

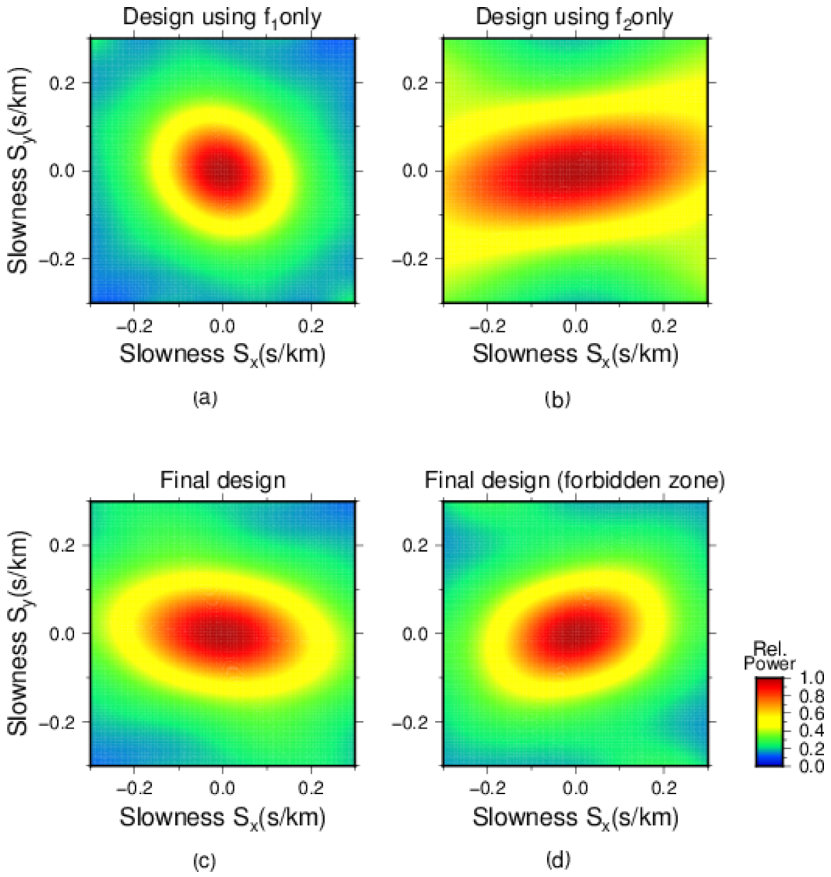

Figure 13. ARFs of the arrays shown in Fig. 9.

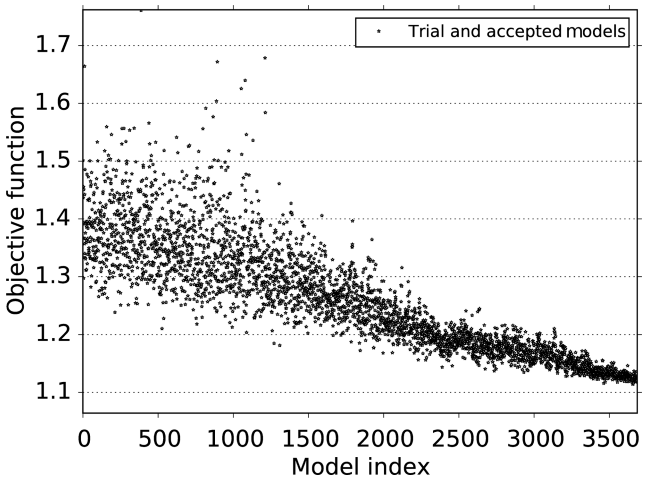

Figure 14. Variation of the final objective function for random models generated and tested in the optimization process. According to the initial set-up of the optimization process, the first 500 models are randomly chosen, while the later models are generated by perturbing some guiding models. The amplitude of model perturbation is reduced in each iteration.

while at the final iterations the selected guiding models change little. The locations of the individual tested models in the objective function space are shown in Fig. 15, where the white star indicates the final optimized solution. In this figure, the value of the final objective function is represented by the colour bar.

3.3.3 *More constraints: forbidden zone*

We imposed a hypothetical condition to the scenario, that is, the existence of a forbidden zone in the deployment site that should be excluded in the model sampling. Such a forbidden zone is realized for instance because of ownership issues. The assumed forbidden zone is marked with a rectangle in Fig. 9(d). The final optimum geometry (Fig. 9c) has already two stations situated in the forbidden zone. So the optimization algorithm has to find another distribution of stations considering this geometrical limitation. The new solution is depicted in Fig. 9(d), and the corresponding point in the objective function space is shown in Fig. 15. The corresponding co-array and the ARF of this geometry are shown in Figs 12(d) and 13(d). For the spatial distribution of the family of solutions for each station see Fig. 16. The performance of two final geometries (black and white stars in Fig. 15) are quite the same in terms of the objective function related to the array beam power, f_1, and the final geometry with forbidden zone is slightly better than the other one in terms of the objective function related to the accuracy of slowness vector, f_2.

Although in this example we used a rectangular shape as a forbidden zone, the algorithm is flexible to consider an arbitrary shape and a number of forbidden zones.

3.3.4 *Comparing with regular geometries*

We evaluated the objective functions for some well-known regular arrays to compare with the final solutions suggested in this study. Regular shape arrays are depicted in Fig. 17 and the values of the

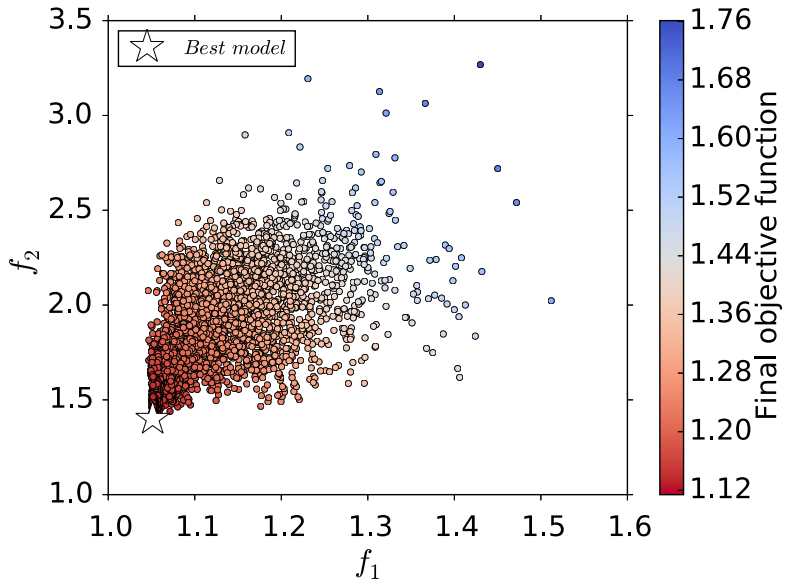

Figure 15. Values of individual tested models in the objective function space, for which the convergence pattern is shown in Fig. 14. The white star indicates to the final model. The colour bar represents the value of the final objective function.

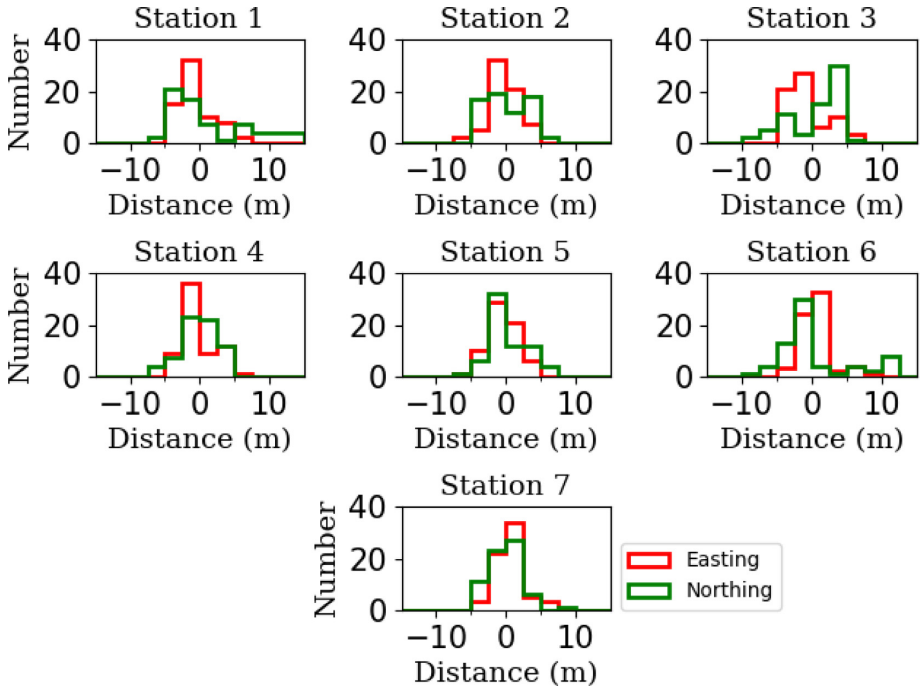

Figure 16. Histograms of the spatial distribution of family of solutions for the geometry shown in Fig. 9(d). For each station the red line shows the distribution of distances in east–west direction relative to the average location and the green line illustrates the same values in the north–south direction. Station numbers are in agreement with the station order in Fig. 9(d).

objective functions are shown in Fig. 18. In addition the Vogtland array (Fig. 3b) is included in this comparison.

We concluded that, the final arrays that are suggested for the region using introduced scenario and boundary conditions perform better than the other arrays in terms of f_2 (precise slowness vector). However, a uniform array geometry, shown in Fig. 17(d), can perform better than the others in terms of the objective function f_1 (array beam power). Such an array gives approximately the same value of the objective function f_2 as both circular arrays with and without a station in the centre. The spiral-arm shaped array and the Vogtland array operate rather similarly for both objective functions.

3.3.5 *Robustness of the optimization method*

We did an experiment to test the robustness of the optimization process by running it 200 times and analysing the minimum value

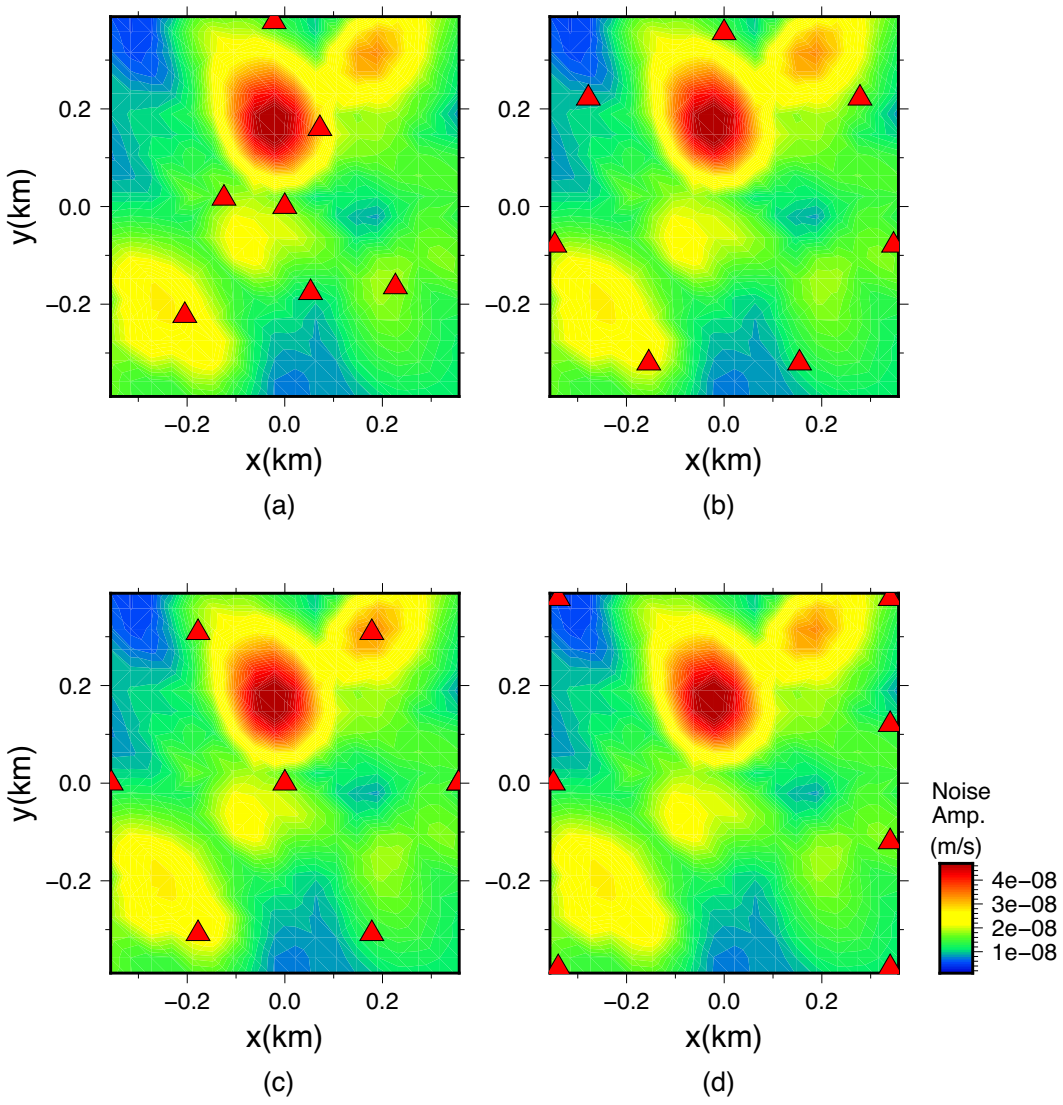

Figure 17. Examples of seven-station regular arrays, spiral arms (a), circular (b), circular with centre (c) and two uniform lines (d), which are used for comparison with the final optimized array. Corresponding values of the objective functions are shown in Fig. 18.

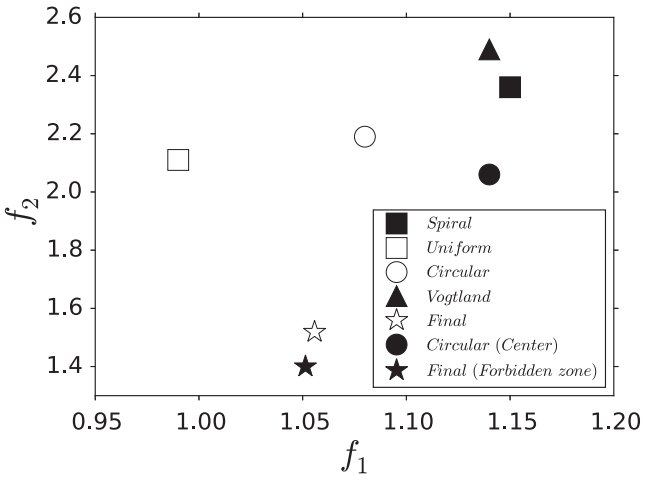

Figure 18. Comparing the performance of the final suggested arrays (white and black stars) with regular geometries depicted in Fig. 17 and the Vogtland array shown in Fig. 3(b).

Table 3. Input parameters to set up ARF as an objective function.

Parameter	Value
Frequency band	2–8 Hz
Slowness range	± 0.3 s km^{-1}
Number of slowness grids	200
Number of stations	$N = 7$

of the objective function obtained in every run. In this test, to decrease the calculation time, we used the theoretical ARF (eq. 1) as the objective function with the set-up parameters as summarized in Table 3. The set-up parameters for the optimization program are the same as the optimizations using the other objective functions discussed in this paper and are already introduced in Table 2.

In Fig. 19, for each experiment, the minimum values of the objective function calculated from the initial random population (circles) and the optimization process (dots) are plotted. From the results we conclude that, as we repeat the optimization process, while the final solutions are not always the same, the minimum value of the objective function remains in the same level. In addition, this figure indicates that, since the improvement of the minimum value of the

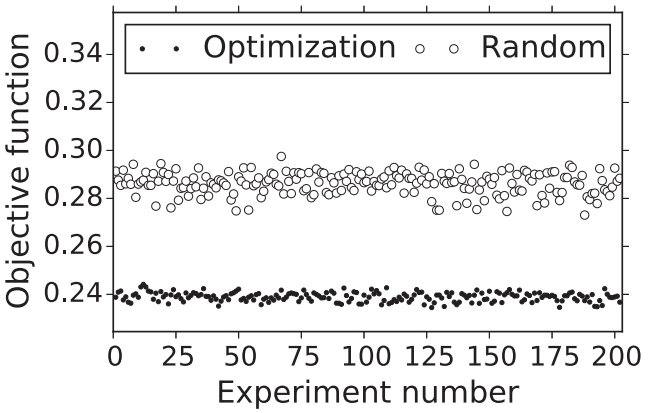

Figure 19. Results of repeating the optimization process using the same initial conditions. The ARF is used as objective function. Circles mark the minimum value of the initial populations that are randomly drawn, and black dots are the minimum value of the objective function obtained during the optimization process.

objective function from a random population to the final optimized solution is almost consistent, the general trend of the convergence remains the same if we repeat the experiment.

In practice, it is a useful property of the algorithm that it can suggest several geometries with approximately the same performance. Accordingly, the user can decide to deploy an array geometry based on the unforeseen circumstances at the deployment site.

3.4 Conclusion

In this study, we have developed an array design framework that provides a flexible tool to perform an automatic search for an optimized array geometry. The framework implements a customizable scenario modelling and optimization scheme. The main point of this framework is to use realistic synthetic seismograms, which makes it possible to take into account ranges of possible source mechanisms, geometry of the seismogenic zone, propagation velocities and noise levels at potential deployment sites. The synthetic array data are then used to evaluate one or more objective functions to be minimized during the optimization process. The objective functions can be defined by user preference based on the monitoring goals.

We showed an example of a seven-station array design in a swarm activity zone in Northwest Bohemia/Vogtland area. By presenting this example, our aim is to show how the array design framework can be initialized and customized for a specific problem. The parameters needed for the synthetic array waveform modelling are derived from previous seismological studies of this region added by realistic estimation of synthetic noise. The synthetic noise level is estimated from real samples of waveforms recorded by an array that was installed temporarily in the same area (Fig. 3b).

Two objective functions are introduced to ensure the accuracy of the estimated *P*- and *S*-phase slowness of synthetic signals. Using the scalarization technique, two objective functions are combined in one single function and a final optimized geometry is introduced.

By a statistical robustness test of applied optimization process, we conclude that if we rerun the algorithm with the same initial set-up, while the final model is not unique, the related value of the objective function remains almost the same. In other words, it is possible to make more than one suggestion with similar performance in terms of the defined objective function.

ACKNOWLEDGEMENTS

We appreciate the anonymous reviewers and the handling editor for their thorough review and constructive comments and suggestions that significantly improved our paper. We acknowledge the University of Potsdam especially Daniel Vollmer and Matthias Ohrnberger for the data at the temporary array installed in Vogtland.

REFERENCES

Baumgardt, D.R. & Der, Z., 1998. Identification of presumed shallow underwater chemical explosions using land-based regional arrays, *Bull. seism. Soc. Am.,* **88**(2), 581–595.

Ben-Menahem, A. & Beydoun, W.B., 1985. Range of validity of seismic ray and beam methods in general inhomogeneous media—I. General theory, *Geophys. J. Int.,* **82**(2), 207–234.

Bondár, I., North, R.G. & Beall, G., 1999. Teleseismic slowness-azimuth station corrections for the international monitoring system seismic network, *Bull. seism. Soc. Am.,* **89**(4), 989–1003.

Büttner, G., Feranec, J., Jaffrain, G., Mari, L., Maucha, G. & Soukup, T., 2004. The Corine Land Cover 2000 Project, *EARSeL eProc.,* **3**(3), 331–346.

Caramia, M. & Dell' Olmo, P., 2008. Multi-objective Management in Freight Logistics: Increasing Capacity, Service Level and Safety with Optimization Algorithms, in *Multi-objective optimization,* pp. 11–36, Springer.

Dahm, T., Horálek, J. & Šílený, J., 2000. Comparison of absolute and relative moment tensor solutions for the January 1997 west Bohemia earthquake swarm, *Stud. Geophys. Geod.,* **44**(2), 233–250.

Dahm, T., Fischer, T. & Hainzl, S., 2008. Mechanical intrusion models and their implications for the possibility of magma-driven swarms in NW Bohemia Region, *Stud. Geophys. Geod.,* **52**(4), 529–548.

Fischer, T. & Horálek, J., 2003. Space-time distribution of earthquake swarms in the principal focal zone of the NW Bohemia/Vogtland seismoactive region: period 1985–2001, *J. Geodyn.,* **35**(1-2), 125–144.

Fischer, T., Horálek, J., Michálek, J. & Boušková, A., 2010. The 2008 West Bohemia earthquake swarm in the light of the WEBNET network, *J. Seismol.,* **14**(4), 665–682.

Ghosh, A., Vidale, J.E., Sweet, J.R., Creager, K.C. & Wech, A.G., 2009. Tremor patches in Cascadia revealed by seismic array analysis, *Geophys. Res. Lett.,* **36,** 1–5.

Hainzl, S., Fischer, T., Čermáková, H., Bachura, M. & Vlček, J., 2016. Aftershocks triggered by fluid intrusion: evidence for the aftershock sequence occurred 2014 in west Bohemia/Vogtland, *J. geophys. Res.,* **121**(4), 2575–2590.

Hardt, M. & Scherbaum, F., 1994. The design of optimum networks for aftershock recordings, *Geophys. J. Int.,* **117**(3), 716–726.

Haubrich, R.A., 1968. Array design, *Bull. seism. Soc. Am.,* **58**(3), 977–991.

Heimann, S. *et al.*, 2017. Pyrocko—an open-source seismology toolbox and library. V.0.3, Online data, GFZ Data Services, do:10.5880/GFZ.2.1.2017.001.

Hensch, M., Riedel, C., Reinhardt, J. & Dahm, T., 2008. Hypocenter migration of fluid-induced earthquake swarms in the Tjörnes Fracture Zone (North Iceland), *Tectonophysics,* **447**(1-4), 80–94.

Hiemer, S., Rüssler, D. & Scherbaum, F., 2012. Monitoring the West Bohemian earthquake swarm in 2008/2009 by a temporary small-aperture seismic array, *J. Seismol.,* **16,** 169–182.

Horálek, J. & Šílený, J., 2013. Source mechanisms of the 2000 earthquake swarm in the West Bohemia/Vogtland region (Central Europe), *Geophys. J. Int.,* **194**(2), 979–999.

Horálek, J., Fischer, T., Boušková, A., Michálek, J. & Hrubcová, P., 2009. The West Bohemian 2008-earthquake swarm: when, where, what size and data, *Stud. Geophys. Geod.,* **53**(3), 351–358.

Ishii, M., 2011. High-frequency rupture properties of the M_w 9.0 off the Pacific coast of Tohoku Earthquake, *Earth Planets Space,* **63,** 609–614.

Kennett, B. L.N., Stipčević, J. & Gorbatov, A., 2015. Spiral-arm seismic arrays, *Bull. seism. Soc. Am.,* **105**(4), 2109–2116.

Kim, S.G., Park, Y.C. & Kim, W.Y., 1998. Discrimination of small earthquakes and artificial explosions in the Korean Peninsula using *Pg*/*Lg* ratios, *Geophys. J. Int.,* **134**(1), 267–276.

Krüger, F. & Ohrnberger, M., 2005. Tracking the rupture of the $M_w = 9.3$ Sumatra earthquake over 1,150 km at teleseismic distance, *Nature,* **435,** 937–939.

La Rocca, M., Galluzzo, D., Malone, S., McCausland, W., Saccorotti, G. & Del Pezzo, E., 2008. Testing small-aperture array analysis on well-located earthquakes, and application to the location of deep tremor, *Bull. seism. Soc. Am.,* **98**(2), 620–635.

Laponce, J., 1972. Vilfredo Pareto, Manual of Political Economy. Trans. Ann S. Schwier, ed. Ann S. Schwier and Alfred N. Page. New York: Augustus M. Kelley, 1971, pp. xii, 504., *Can. J. Political Sci.,* **5**(04), 599–600.

Larsen, C.H., 2012. Reports on deep Earth sampling and monitoring, *Sci. Drill.,* **14,** 1–80.

Málek, J., Jansky, J., Novotný, O. & Rüssler, D., 2004. Vertically inhomogeneous models of the upper crustal structure in the West-Bohemian seismoactive region inferred from the celebration 2000 refraction data, *Stud. Geophys. Geod.,* **48**(4), 709–730.

Málek, J., Horálek, J. & Jansky, J., 2005. One-dimensional qP-wave velocity model of the upper crust for the West Bohemia/Vogtland Earthquake swarm region, *Stud. Geophys. Geod.,* **49**(4), 501–524.

Marano, S., Fah, D. & Lu, Y.M., 2014. Sensor placement for the analysis of seismic surface waves: sources of error, design criterion and array design algorithms, *Geophys. J. Int.,* **197**(3), 1566–1581.

Marler, R.T. & Arora, J.S., 2004. Survey of multi-objective optimization methods for engineering, *Struct. Multidiscip. Optim.,* **26**(6), 369–395.

Meng, L., Allen, R.M. & Ampuero, J.-P., 2014. Application of seismic array processing to earthquake early warning, *Bull. seism. Soc. Am.,* **104**(5), 2553–2561.

Morita, Y., Nakao, S. & Hayashi, Y., 2006. A quantitative approach to the dike intrusion process inferred from a joint analysis of geodetic and seismological data for the 1998 earthquake swarm off the east coast of Izu Peninsula, central Japan, *J. geophys. Res.,* **111**(6), 1–18.

Neunhöfer, H. & Hemmann, A., 2005. Earthquake swarms in the Vogtland/Western Bohemia region: spatial distribution and magnitude–frequency distribution as an indication of the genesis of swarms?, *J. Geodyn.,* **39**(4), 361–385.

Okabe, A., Boots, B. & Sugihara, K., 1992. *Spatial Tesselation: Concepts and Applications of Voronoi Diagrams,* John Wiley and Sons.

Passarelli, L. *et al.*, 2015. Aseismic transient driving the swarm-like seismic sequence in the Pollino range, Southern Italy, *Geophys. J. Int.,* **201**(3), 1553–1567.

Rost, S. & Thomas, C., 2002. Array seismology: methods and applications, *Rev. Geophys.,* **40**(3), 1–2.

Růzek, B. & Horálek, J., 2013. Three-dimensional seismic velocity model of the west Bohemia/Vogtland seismoactive region, *Geophys. J. Int.,* **195**(2), 1251–1266.

Saccorotti, G. & Del Pezzo, E., 2000. A probabilistic approach to the inversion of data from a seismic array and its application to volcanic signals, *Geophys. J. Int.,* **143**(1), 249–261.

Sambridge, M., 1999. Geophysical inversion with a neighbourhood algorithm—I. Searching a parameter space, *Geophys. J. Int.,* **138**(2), 479–494.

Schweitzer, J., Fyen, J., Mykkeltveit, S. & Kværna, T., 2012. Seismic Arrays, in *New Manual of Seismological Observatory Practice 2 (NMSOP-2),* pp. 1–80, ed. Bormann, P., GFZ German Research Centre for Geosciences.

Sen, M.K. & Stoffa, P.L., 2013. *Global Optimization Methods in Geophysical Inversion,* Cambridge Univ. Press.

Wathelet, M., 2008. An improved neighborhood algorithm: parameter conditions and dynamic scaling, *Geophys. Res. Lett.,* **35**(9), 1–5.

Wathelet, M., Jongmans, D., Ohrnberger, M. & Bonnefoy-Claudet, S., 2008. Array performances for ambient vibrations on a shallow structure and consequences over V_s inversion, *J. Seismol.,* **12**(1), 1–19.